

Image Analysis for the Study of Radionuclide Distribution in Tissue Sections

J.L. Humm, R.M. Macklis, Y. Yang, K. Bump and L.M. Chin

Joint Center for Radiation Therapy, Harvard Medical School, Boston, Massachusetts

Tissue section autoradiographs are often prepared to review the precise spatial locations of a radiolabeled molecule relative to cells, such as in the study of radiolabeled antibody distribution. The objective of this work was to develop and evaluate a method to automatically detect both grains and cell nuclei from stained tissue autoradiographs using a microscope and an image analyzer. **Method:** Using a sequence of morphological image operations, the densely stained regions of the section, representing the cell nuclei are identified first, and then subtracted from the original image. This enables the identification of autoradiographic grains under conditions of variable contrast, by separation of the grains overlapping the cell nuclei from the extracellular spaces, permitting a more accurate and robust automatic segmentation routine. **Results:** The accuracy of the method to detect grains has been evaluated at different threshold levels. The highest accuracy obtained was approximately 90%. The accuracy in the detection of cell nuclei was histology-dependent. As examples, we have estimated accuracies of approximately: 86%, 81% and 77% for kidney, EL-4 lymphoma and pneumonocyte sections, respectively. **Conclusion:** This method was tested using specimens designed to study radiolabeled antibody distribution, but it should be applicable with comparable accuracy to other radiolabeled compounds for which quantitative information on the heterogeneity of distribution is required.

Key Words: autoradiography; microdosimetry; image analysis

J Nucl Med 1994; 35:1217-1225

When radiolabeled molecules are used for targeting therapy, e.g., radiolabeled antibodies (1-6), thymidine precursors (7-9), methylene blue (10,11), naphthoquinone derivatives (12), hormones (13) etc., it is important to obtain detailed information on the spatial distribution of the sources relative to the cells, so that the uniformity of uptake and dose to the tumor cells can be assessed. Autoradiography is a method to obtain precise spatial information (resolution $\leq 1 \mu$) of the radiolabels, relative to the tissue histology. Theoretical studies have shown (14,15) the necessity to determine the spatial configuration of sources with this level of spatial resolution, if accurate estimates of

the cell doses are to be obtained. For example, a 1- μ m error in the spatial registration of an alpha source at the position of the cell membrane can result in a 20% error in the dose delivered to the cell nucleus (16). Although autoradiography only provides information at a single time point, it is the only current technique capable of providing spatial source distribution with subcellular precision.

The large volume of data present on an autoradiograph necessitates automated methods of data collection. Previous researchers have used microdensitometry to quantify the activity distribution across tissue sections (17-19). This method, although rapid, presents the investigator with a matrix of grain densities devoid of its relation to the cellular structure of tissue. This can result in errors, since the activity and dose distribution are not associated with the distribution of viable cells across the section.

We present a method of automatic grain and cell nucleus recognition from autoradiographs using image analysis. The method is demonstrated using examples of the localization of radiolabeled antibodies in tumor tissue.

METHODS

Tissue Section Autoradiography

Autoradiographs were prepared from three tissue blocks. An EL-4 T-cell lymphoma-bearing mouse was injected with 11.1 MBq of ^{111}In -labeled Thy 1.2 tumor-specific antibody, and killed after 24 hr. The tumor was excised, and embedded in LKB historesin. The tumor tissue sections were cut on a Microm 330 resin microtome, (Heidelberg, Germany) dipped in Ilford K2 emulsion and exposed for 1 wk, prior to development. Then these sections were stained with Harris's hematoxylin. The second autoradiograph was of a kidney section from the same animal. The third autoradiograph was from a lung tumor (a type II pneumonocyte, provided by courtesy of L.M. Cobb, MRC Radiobiology Unit, Didscot, Oxon, England), which had been injected with a ^{125}I -labeled nonspecific Thy 1.1 antibody and killed 6 hr postadministration. This tissue was paraffin embedded. Sections were dipped in Ilford K2 emulsion, exposed for 2 wk prior to development, then stained in hematoxylin and eosin.

Since both ^{111}In and ^{125}I are Auger electron emitters, the half-density of the grain position relative to the source decay is $\leq 1 \mu\text{m}$ (20).

Image Acquisition

Tissue sections were viewed on a Reichert Jung Polyvar microscope (Vienna, Austria) under Kohler illumination. A black and white (512 \times 480) Cohu CCD camera (San Diego, CA) mounted on the microscope tube was used to digitize the images.

Received Oct. 6, 1993; revision accepted Mar. 4, 1994.
For correspondence or reprints contact: J. L. Humm, PhD, Dept. of Medical Physics, Memorial Sloan-Kettering Cancer Center, 1275 York Ave., New York, NY 10021.

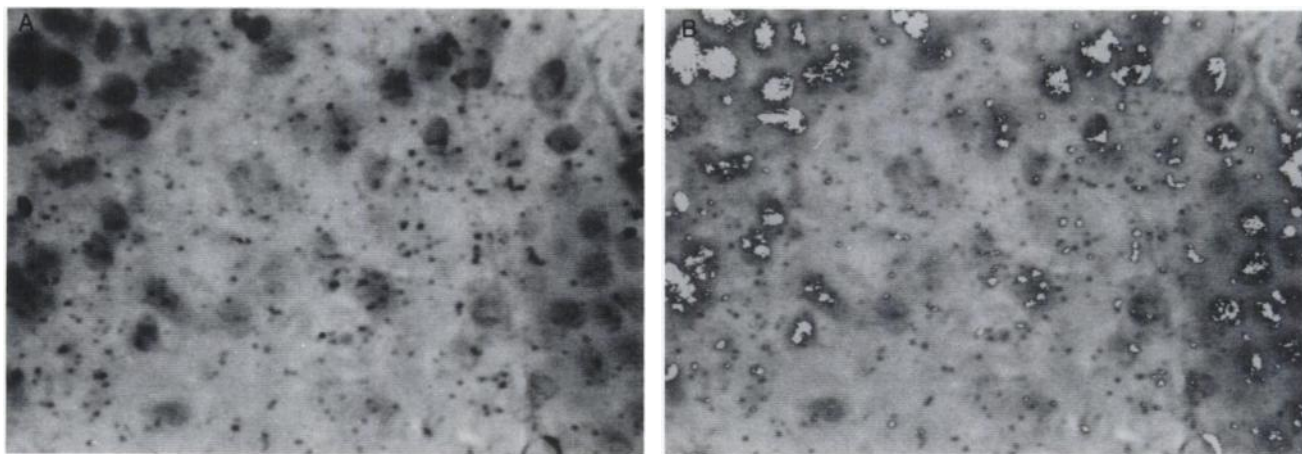


FIGURE 1. (A) A digitized black and white image of an EL-4 tumor autoradiograph stained with Harris's hematoxylin, 24 hr post-intravenous tail vein injection with ^{111}In -labeled Thy 1.2 antibody. The magnification is 500x. (B) An attempt to detect the autoradiographic grains by grey level thresholding. Objects below the grey level threshold are highlighted in white. This technique fails, since not only do many grains remain undetected, but many densely stained areas of the hematoxylin-stained nuclei are erroneously confused for grains.

The camera gain and offset were adjusted to spread the image contrast across the full 256 grey levels, without camera saturation. Using a magnification of 500x for visualization of the autoradiographic grains, the camera field of view was $150 \times 140 \mu\text{m}^2$ (calibrated with a hemocytometer) corresponding to $0.3 \mu\text{m}/\text{pixel}$. Image analysis was performed using a Quantimet 570-PC based image analyzer (Leica, Deerfield, IL). Nonuniformity of specimen illumination was corrected using a matrix-shading correction derived from a blank image. Corrections for the pixel nonsquareness were performed in real time using look-up-tables (LUT).

Image Analysis Method to Detect Cell Nuclei and Autoradiographic Grains

Figure 1A shows an image acquired on the black and white camera of an autoradiograph of the EL-4 T-cell lymphoma. Since the autoradiographic grains ride on a background of variable staining, simple grey level thresholding cannot be used for grain segmentation as demonstrated in Figure 1B. Even when the grain/background contrast is considerably more uniform, as with a kidney section, grey level segmentation still failed. This failure is due to the considerable overlap of grains and cell nuclei in the grey level windows. Therefore, our approach has been initially to detect the cell nuclei and then to break the original image into two separate images, one containing only the cell nuclei, and the second containing only the background. Grain detection is then performed in the extra- and intra-cell nuclear regions separately.

A detailed description of the steps involved in the identification of the cell nuclei and autoradiographic grains is given in the Appendix. A schematic diagram of the steps involved in cell nuclei recognition is shown in Figure 2, and the appearance of the images for these steps is deferred to the Appendix. In brief, the original image is smoothed to eliminate small objects such as grains from the image, but not the larger individual cell nuclei. All local minima in the smoothed image are sought, to identify the deepest stained areas of the section (Fig. 2B). These minima are progressively dilated, according to a grey level ramp, until a set of ridge lines of maximum grey level intensity between all detected minima are found (Fig. 2C). This filter is the watershed function (21,22). The watershed ridge lines are segmented by grey level thresholding, and set to zero (black). A gradient filter is applied to the original image to enhance the cell nuclear boundaries (Fig.

2D). The black watershed lines and the minima from Figure 2C are copied onto the gradient image in Figure 2D to produce Figure 2E. Application of a second watershed causes the darkest pixels of the image (the cell nuclei minima and the watershed lines) to dilate and converge onto the boundaries of maximum grey level pixels which are the gradient lines. The result is illustrated in Figure 2F. By hole filling and removal of the watershed lines, the cell nuclei are detected, and the objects without closure removed.

A mask of the detected nuclei is created which is used to create two new images: one which copies the contents of the original image of only those pixels underlying the mask, and a second which copies the remainder of the original image.

The intra-nuclear grains are identified by smoothing the image of the cell nuclei and identifying local minima. The extra-nuclear

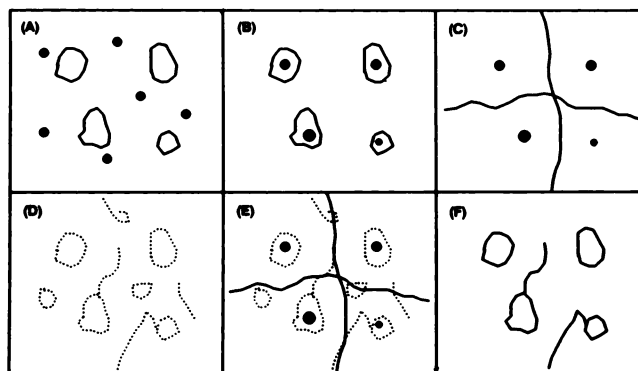


FIGURE 2. (A) Schematic diagram of an image containing the outlines of cell nuclei and autoradiographic grains (black dots). (B) The operation of smoothing removes the autoradiographic grains. The search for local image minima detects the deepest stained areas within the cell nuclei (filled black areas). (C) The watershed lines derived from the image minima (filled black areas) of 2B. (D) The outlines of objects using gradient analysis of the original image. (E) Superposition of the image minima and watershed lines from 2C onto the gradient image of 2D. (F) Result of the second application of the watershed function. The minima grow outward and the first set of watershed lines grow inward. The two meet at the gradient lines. The enclosed watershed lines contain cell nuclei. The extraneous lines are readily pruned from the image.

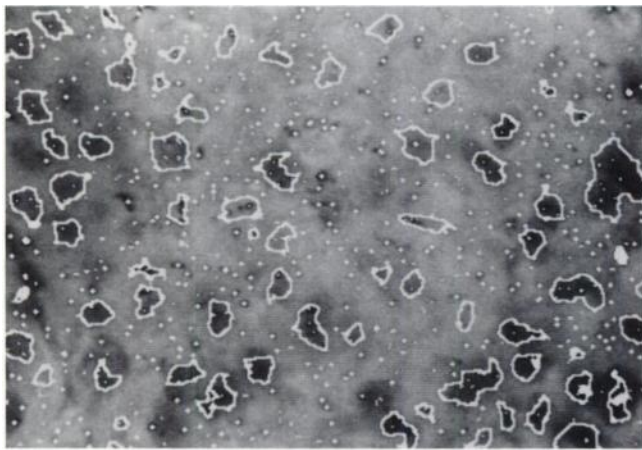


FIGURE 3. Image of the detected extra- and intranuclear grains, together with the outlines of the detected cell nuclei highlighted in white for the unprocessed EL-4 T-cell lymphoma section shown in Figure 1A, after applying the image analysis procedures described in the appendix.

grains are identified by size and grey level thresholding which are combined in the top-hat transform, which isolates all grey level minima from the image smaller in size than the specified grey level opening kernel.

RESULTS

The Accuracy of Automatic Grain Recognition

The results of applying the image analysis techniques to identify grains and cell nuclei are illustrated for the three histologies in Figures 3, 4 and 5. The accuracy of the method was evaluated by toggling the binary planes containing the detected grains and cell nuclei on and off. Three independent observers manually scored the number of true-positives, false-positives and undetected features.

Two operator variables define the accuracy of grain identification: the size of the kernel used in the top-hat transform and the grey level threshold applied to the re-

sultant image. The top-hat transform is a difference image between the original image and grey level opened image. A grey level opening is an image erosion followed by an image dilation of equal magnitude determined by the kernel size (22). An image opening removes small features from the image, by eroding them to nothing, so that they cannot be reconstituted by dilation. Therefore, the application of the top-hat transform sets all image pixels of smoothly varying objects equal to zero (black), and highlights small sharp features, such as autoradiographic grains, of sizes less than the radius of the user-defined kernel to high grey level values (220–255). The choice of the top-hat kernel depends upon the optical magnification used. At 500x magnification, typical grain sizes were 4–16 pixels in area. The optimum kernel size corresponds to the size of features requiring detection. In this work, a kernel of size 2 was used, although the method was insensitive within the range from 2 to 4 inclusive.

Second and more critical is the white threshold level for segmentation of the grains from the top-hat transformed image. The grey level stores from 255 down to 220 contain the distribution of individual grain data in the order of diminishing contrast relative to their individual backgrounds. Therefore, opening the grey level window by decreasing the threshold level results in an increase in the true grain count, but at the expense of a rapid increase in the yield of false-positives. This is because each incremental lowering of the threshold, (widening of the window) results in a progressive lowering of the signal (true grain count) to noise (false-positives). To investigate the dependence of true-positives upon threshold level, we used the method of Giger et al. (23). In a study of an automated detection method for the identification of malignant lesions in lung from radiological films, they presented the performance of their technique by plotting the incidence of true-positives versus false-positives as the thresholding level was changed. This method, which is similar to a receiver-

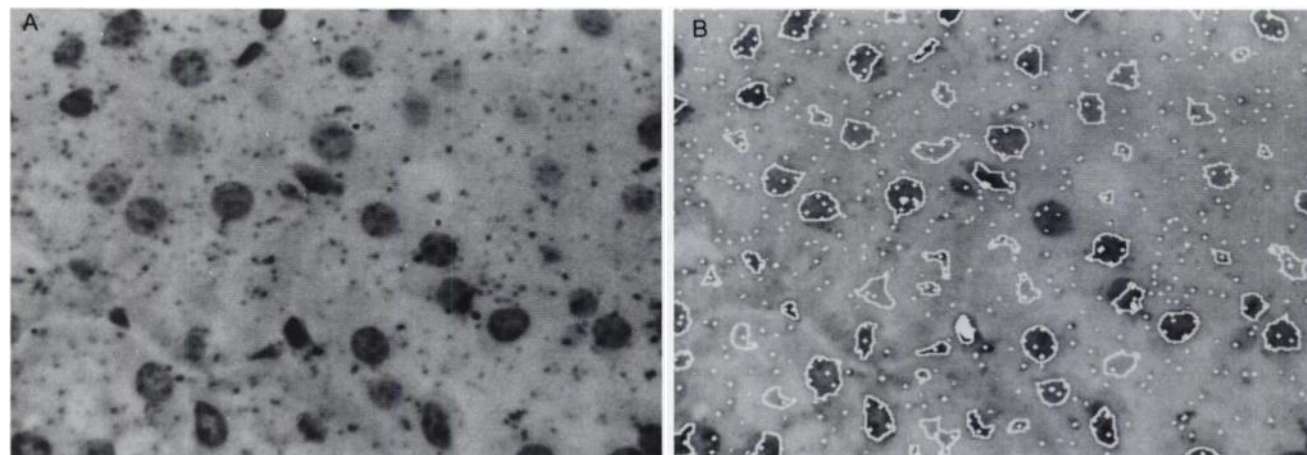


FIGURE 4. (A) A digitized black and white image of an autoradiograph of a kidney section stained with Harris's hematoxylin, 24 hr postintravenous tail vein injection with ^{111}In -labeled Thy 1.2 antibody. The magnification is 500x. (B) The same image after applying the image analysis procedures described in the Appendix. The detected cell nuclei are outlined in white. The detected autoradiographic grains are highlighted as white dots.

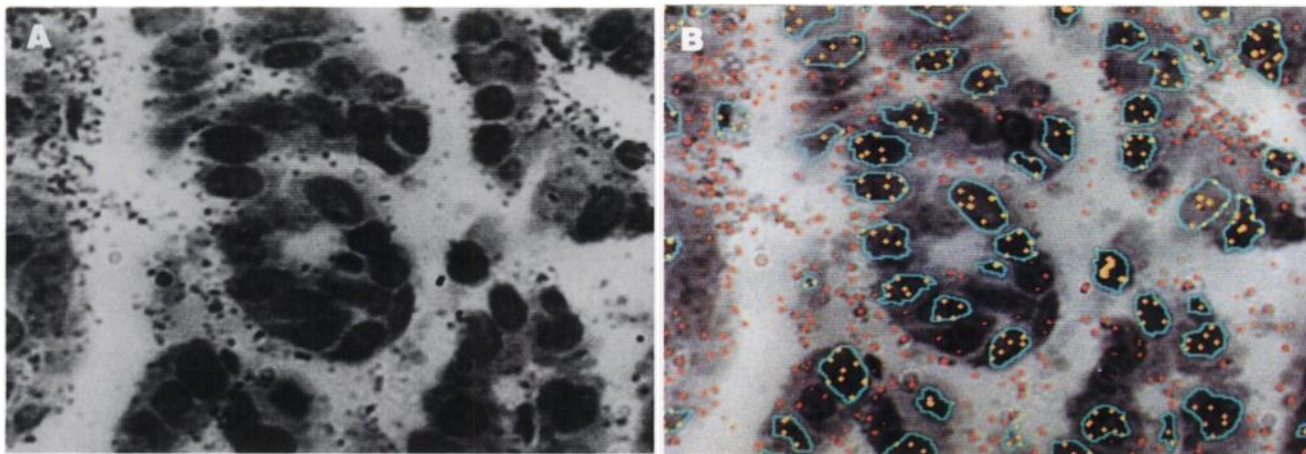


FIGURE 5. (A) A digitized black and white image of an autoradiograph of a type II pneumonocyte tumor section stained with hematoxylin. The magnification is 500x. (B) Application of the image analysis technique described for the EL-4 tumor section applied to a pneumonocyte type II tumor section. Detected cell outlines are shown in turquoise, extra-nuclear grains in red, and intranuclear grains in yellow.

operator characteristic (ROC) curve in radiology, describes the sensitivity and behavior of the method. Figure 6 presents data for the automatic grain detection method, where each filled circle represents a change in the grey level threshold by 1/256. The ordinate gives the percentage of true-positives; the abscissa, the percentage of false-positives relative to the true number of grains (1,140 normalized to 100% in the figures) analyzed. Figure 6 shows that we can extract 85% of the grains with less than 1% of false-positive grains. In order to improve the detection level to greater than 95% of the true grains, the percentage of false-positives increased to about 5%. At this point the overall grain count is close to 100%, since the percentage of false-positives closely matches the percentage of undetected grains. However, 5% of the grain coordinates are erroneous. Increasing the thresholding level higher results in

an unacceptable rise in the number of false-positives with only a small improvement in the detection of the missing grains. The curve in Figure 6 allows one to determine the optimum threshold for minimizing the joint error arising from undetected and false-positive components, to a point just before the large increase in false-positives.

Although the accuracy of the method is sensitive to the grey level threshold, this threshold needs to be determined only once for each specimen, since the top-hat transform is insensitive to the absolute grey level intensity of the background. All large features in the image disappear during image subtraction and are set to a grey level equal to zero. For example, changing the illumination in the linear response range of the camera, results in a change in the overall brightness and contrast of the image, but has little effect on the threshold levels required to segment grains from the top-hat transformed image. What may change, with the absolute illumination intensity, is the level of noise detected. However, since noise is a single-pixel phenomenon, it is easily removed by size thresholding, i.e., only objects consisting of four or more adjacent pixels are counted as grains. Therefore, fluctuations in noise at different illumination levels are minimal. This method therefore has distinct advantages over techniques which employ conventional grey level thresholding, where measurements upon the same field may vary significantly dependent on the overall specimen brightness.

Using the optimum settings for grain thresholding (determined from Fig. 6), the number of positively and falsely detected grains from 1,140 individual grains are presented in Table 1.

The data demonstrate the high accuracy of individual grain identification. However, the method is limited to individual grains, and does not detect grain clusters, which are excluded due to the small size threshold applied during the top-hat transform. Grain clusters, if they occur, need to be identified manually.

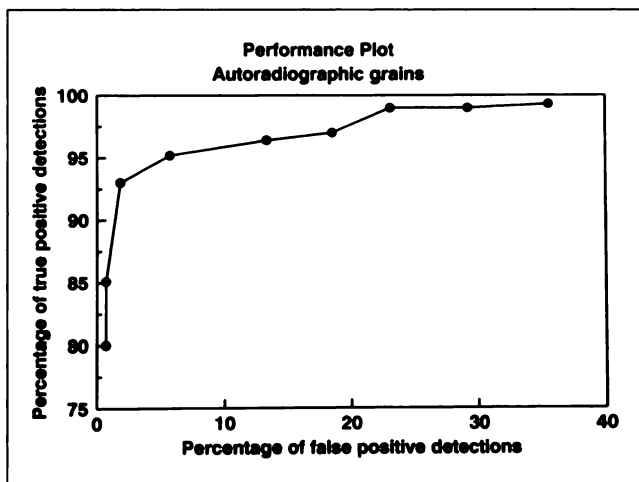


FIGURE 6. The performance characteristics of the automated autoradiographic grain detection method, with the percentage of true-positive identifications on the ordinate versus false-positives on the abscissa, using grey level threshold as the variable. Percentages are expressed relative to the average number of grains identified manually by three independent observers.

TABLE 1
The Accuracy of Automatic Grain and Cell Nuclei Detection
Expressed as the Number of Undetected and
False-positive Objects.

	Number	Undetected	False-positives
Grains	1,140	43	49
EL-4 cell nuclei	745	89	52
Pneumonocyte	861	147	52
Kidney cell nuclei	913	82	46

The Accuracy of Automatic Cell Nucleus Recognition

For the automatic identification of cell nuclei, morphological filters were used exclusively. The size of the kernel of the initial image smoothing operation is the only user-defined variable. This kernel determines the size (the number of adjacent pixels) over which smoothing occurs, and consequently the number of minima or cell nuclei detected from the image. The use of too small a kernel results in insufficient smoothing of the image detail, and the detection of multiple false minima (over-segmentation). The use of too large a kernel results in the elimination of minima corresponding to stained cell nuclei (under-segmentation). We studied the yield of true-positive cell nuclear segmentation versus false-positives for a range of smoothing kernel sizes from 1 to 7 (Fig. 7) for the three tissue types studied. The data are expressed as percentages relative to the true estimate of the cell number (the average of three independent observers) given in Table 1. The rate of loss of true-positive cell nuclei is small for kernel sizes ≤ 4 , but increases rapidly at higher values. Once again, the optimum kernel size compromising between undetected cell nuclei and false-positive cell nuclei falls at the inflection point in Figure 7.

Table 1 shows measured data of the accuracy of cell nuclei recognition for the optimum smoothing kernel size

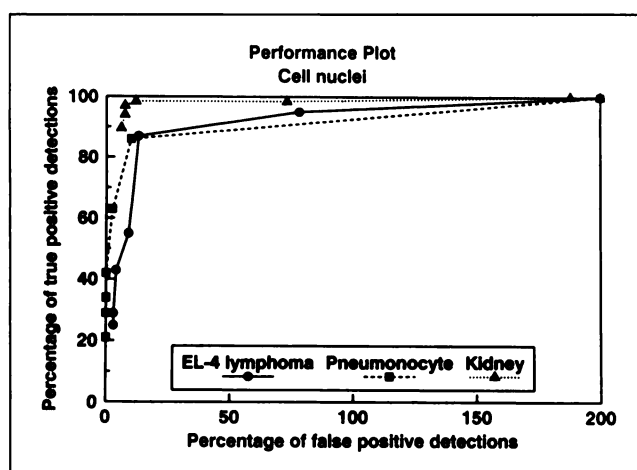


FIGURE 7. Same as Figure 6 showing the performance characteristics of the automated cell nuclei recognition method, with size of the smoothing kernel (ranging from 1 to 7) as the variable. Percentages are expressed relative to the average number of cell nuclei for each histology identified manually by three independent observers.

of 3. The magnitude of the errors are smaller for the normal kidney section than for the two malignant tissues, due to the higher staining contrast obtained for kidney. Like the grey level threshold setting for grain detection, the yield of correctly detected nuclei is a sensitive function of the size of the smoothing kernel. The value of the optimum smoothing kernel was found to be constant for the three histologies studied in this work. This is probably because the variation in size of all mammalian cell nuclei is small. Therefore application of the smoothing kernel to different tissues viewed at the same magnification requires little or no changes to the smoothing kernel, once it is set correctly. The principal limit in the accuracy of the method to segment cell nuclei results from the quality of differential staining which can be achieved between the cell nuclei relative to the non-nuclear material on the section.

For a set of sections derived from the same tissue block and stained in the same batch, the reproducibility of cell nuclei identification is about $\pm 10\%$. This may result from variations in the thickness of the sections, which affects the observed inter-cellular spacing as viewed on a two-dimensional projection. However, larger variations in the detection accuracy of cell nuclei was observed between sections from different blocks. Whereas, for kidney sections, we always obtained better than 75% cell nuclei identification at the optimum level, for the tumor sections from one of four EL-4 resin tumor blocks, the detection efficiency was $< 50\%$. We attribute this to the poorer delineation of the cell nuclei from this specimen arising from the tissue processing and embedding. Obviously inadequate fixation of the specimen will result in poorer quality histology, which is visible by eye, and reflected in the ability to segment cell nuclei.

DISCUSSION

Our motivation for pursuing an accurate assessment of source and target distributions is based on our need to describe the energy distribution at the cellular level in targeted therapy. The success of radiolabeled antibodies for the treatment of malignant disease is highly dependent on the uniformity of the spatial distribution of the radiolabels relative to viable tumor cells. The accuracy with which the spatial coordinates of the sources relative to the target cell nuclei needs to be known is dependent upon the range of action of the radiolabel. For long-range beta-emitters, such as ^{90}Y or ^{32}P , the necessity to obtain the source distribution with micron accuracy is unnecessary for most radiolabel distributions. However, studies with highly specific short-range alpha- and beta-emitters do sanction high spatial resolution data on the source distribution. For Auger emitters whose radiotoxicity may be more than two orders of magnitude greater when incorporated into the cell nucleus compared to decays at extra-nuclear locations, the necessity to separate the image into nuclei and non-nuclei phases, as performed in this study, is essential.

With the image analysis methods presented in this paper,

individual grains were detected with an accuracy of approximately 90% which was constant for a wide range of tissue sections and illumination conditions. Areas of dense grain clusters were not identified by our method and they need to be delineated manually.

Alternative approaches might improve grain detection. One approach might be to analyze the section prior to staining. This would, however, necessitate replacing the section precisely on the stage prior to rescanning for detection of the cell nuclei, and therefore diminish the spatial accuracy between cell nuclei and grains. We did not use this approach, because the potential loss of spatial resolution could be unacceptable for the quantitation of the radiolabeled molecules within the cell nucleus, e.g., the thymidine precursors. An alternative approach was suggested by Eklund and Williams (18) to reduce interference between the histological stain and the silver halide grains. In their work, a quantitative relation of the brightfield-to-darkfield ratio was fitted by a regression relation to the known grain densities determined by manual counting. The disadvantage of this method is that information is lost on the actual positions of the sources and targets, which can be important for some radiolabel configurations (24).

Cell nuclei were detected with an accuracy of between 75% and 85% depending upon the tissue histology and quality of staining. These percentages might be improved with further work, although it is unlikely that major advances will result from software development.

The shortcomings of the current image analysis procedures to identify cell nuclei result from the nonuniformity of stain uptake across the specimen. This results in a complex variation of cell staining intensity and contrast. Investigation into more specific nuclear stains may improve cell nuclei recognition accuracy, but preliminary tests using the more specific Fuelgen cell nuclear stain demonstrated little improvement. The image analysis methodology is applicable to a wide range of tissue stains and staining intensities used in conventional pathology. However, there are limits to the acceptability of the staining intensity. Too weak staining which provides inadequate cell nuclear contrast diminishes the accuracy of cell detection. Too deep staining interferes with the ability to detect grains within cell nuclei. The intrinsic tissue histology was found to be the largest single determinant in limiting the accuracy of automatic cell recognition. For example, the greater spacing between the parenchymal cells of the kidney results in a lower yield of undetected cells than tissues with considerable cell-cell contact, such as for the pneumonocyte tumor. The applicability of the smoothing kernel is re-evaluated for each new tissue type, and adjusted where necessary. In general, the accuracy of cell nuclei detection increases for histologies with greater cell separation.

CONCLUSIONS

In this paper, we presented a method for the automatic detection of autoradiographic grains and cell nuclei from

tissue sections. The procedure was evaluated on three tissue sections of different histology. Results were compared with manual identification. The accuracy of grain identification was approximately 90%. The accuracy of the identification of cell nuclei from three tissue types ranged from 75%–85%, depending on the spatial arrangement and density of the cells. Although the examples shown in this work were of radiolabeled antibody distribution in tissue, these methods can be applied to any radiolabeled compound for which quantitative information of the spatial distribution in tissue is desired. Since this method detects the number and the location of each source point and target cell on the slide, it can be used for uniformity analysis and also for the determination of the distribution of doses at the cellular level.

APPENDIX

Automatic Cell Nuclei Recognition by Image Analysis

The steps involved in the automatic identification of cell nuclei from tissue sections were as follows:

- The original image containing cell nuclei and autoradiographic grains is shown for a real tumor autoradiograph in Figure 1A, and schematically in Figure 2A. To reduce the detail in the grey tone variation across the field, the image is smoothed. This operation eliminates all sharp detail from the image including the grains, leaving a mosaic of coarse grey tone variations.
- All the minima in the smoothed image are sought. This operation corresponds to an adaptive thresholding. The deepest grey tone pixel cluster is identified which approximately corresponds to the deepest stained area of each cell nucleus. The appearance of the image at this point is schematically illustrated in Figure 2B and for the actual EL-4 image in Figure 8A. The smoothing operation has removed the grains from the image and the dark circles now correspond to the grey level minima of the smoothed image representing the deepest stained areas of the cell nuclei. The number of minima in the image corresponds approximately to the number of detected nuclei. This number will depend upon the size of the smoothing kernel and the relation of these parameters is analyzed in the results section.
- The smoothed image is passed through the morphological filter known as the watershed function (21,22). This function takes the pixel minima data and dilates each minimum by successive increments in grey level intensity. The process continues until contact is established between adjacent minima. What remains is a series of boundary lines (the watershed lines) depicting nearest neighbor boundaries (shown schematically in Figure 2C), and for the EL-4 tumor section in Figure 8B. A frequently used analogy of the watershed process is the rising water level in a terrain of mountains and valleys. The valleys will continue to fill until a mountain ridge is reached at which point the water levels of two adjacent valleys meet. The ridge lines connecting these valleys are the watershed lines. For a tissue section, the watershed lines define a set of domains each containing a cell nucleus.
- Neither the watershed lines nor the minima correspond to the boundaries of the cell nuclei. Application of a gradient function on the original image (Fig. 2A) is used to detect the edges of the cell nuclei. However, the grey tone complexity of a

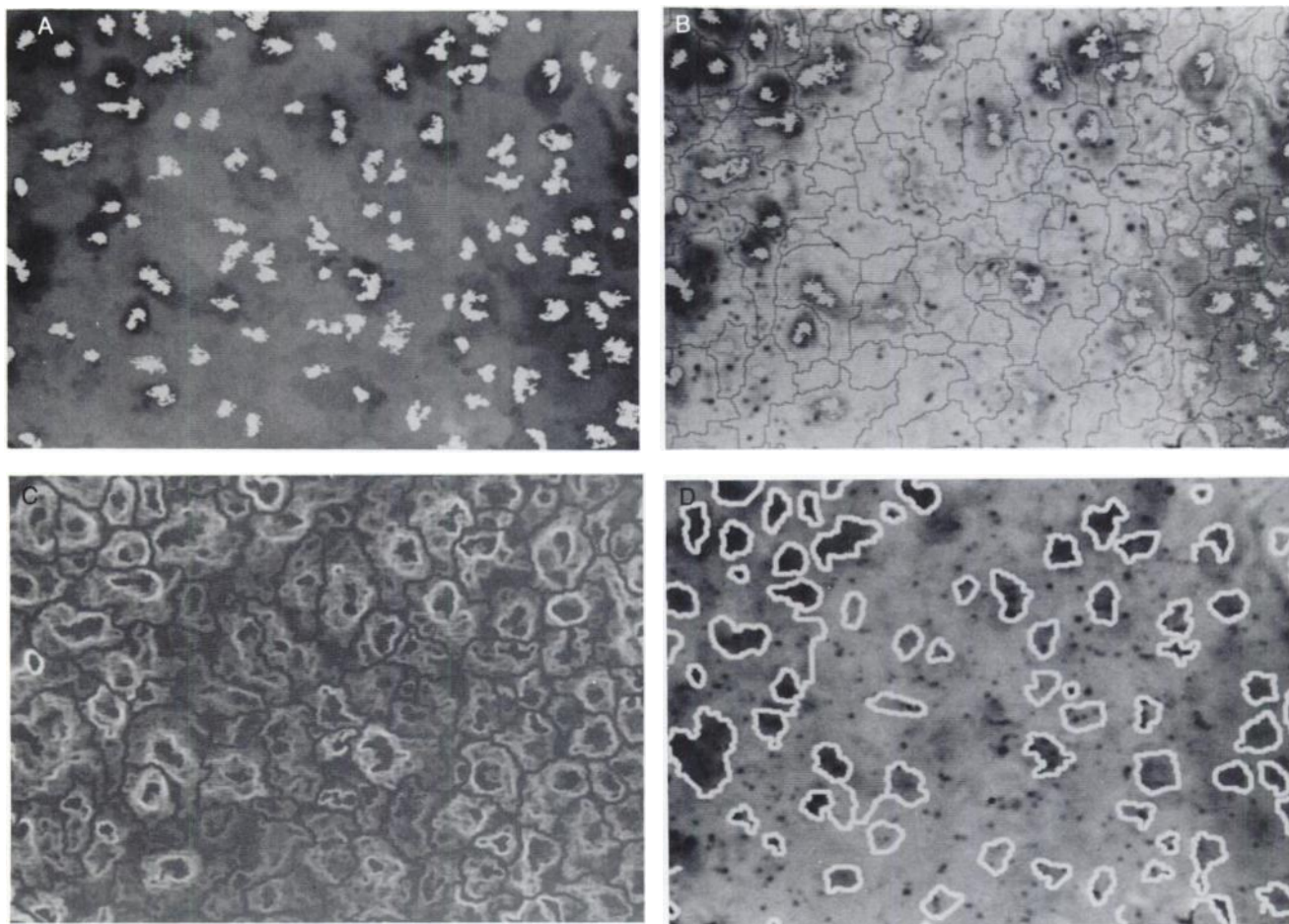


FIGURE 8. (A) Figure 1A after both image smoothing and the search for the local minima. The identified minima, which represent the darkest stained regions of the cell nuclei, are highlighted in white. (B) The watershed lines (black) derived from the image minima (white). (C) Gradient of the original image, with pixels under the masks of the image minima (4A) and watershed lines (4B) set equal to grey level zero (black). (D) Second application of the watershed function to identify the outlines of the cell nuclei (white) overlaid on the original image.

tissue image includes a large number of edges not associated with cell nuclei. The gradient lines are shown schematically by the dotted lines in Figure 2D.

- The image minima and watershed lines are used to clean up extraneous gradient lines. Since the minima and watershed lines can be readily obtained by grey level segmentation, a binary mask of both can be constructed. A mask is an overlay plane which can be used to confine any image operation to only those regions of the image underlying the mask. Using the gradient image of Figure 2D, those pixels underlying the masks of the minima and watershed line masks (Fig. 2C) are set to a grey level 0 (black). This step is illustrated schematically in Figure 2E, and on the EL-4 tumor image in Figure 8C. The modified gradient image now contains well defined maxima (the gradient lines), and well defined minima (the deepest stained regions of the cell nuclei and the watershed lines) both of which were set to grey level 0.
- Application of a second watershed function results in the dilation of the image minima, in accordance with a grey level ramp, until the image maxima. The second set of watershed lines are the solid lines shown schematically in Figure 2F, and for the EL-4 tumor in Figure 8D.

- The second set of watershed lines corresponds closely to the outline of the cell nuclei, but still contains some unwanted lines corresponding to the convergence of the second watershed function to extraneous detail from the gradient image. These lines may be pruned by filling all closed domains within the image and then subtracting the watershed lines. In this way a binary plane is obtained containing only objects with closure. Most of the detected objects correspond to cell nuclei.

The original image (Fig. 1A) is separated into two images; one containing cell nuclei, and one with the cell nuclei subtracted (Fig. 9A and 9B), by copying only the pixels either underneath or outside of the segmentation mask of the cell nuclei. Methods of grain identification can now be performed separately on the two images with a diminished interference between the black extra-nuclear grains and the densely stained areas of the cell nuclei.

Automatic Grain Recognition by Image Analysis

The steps involved in the automatic identification of autoradiographic grains are now presented.

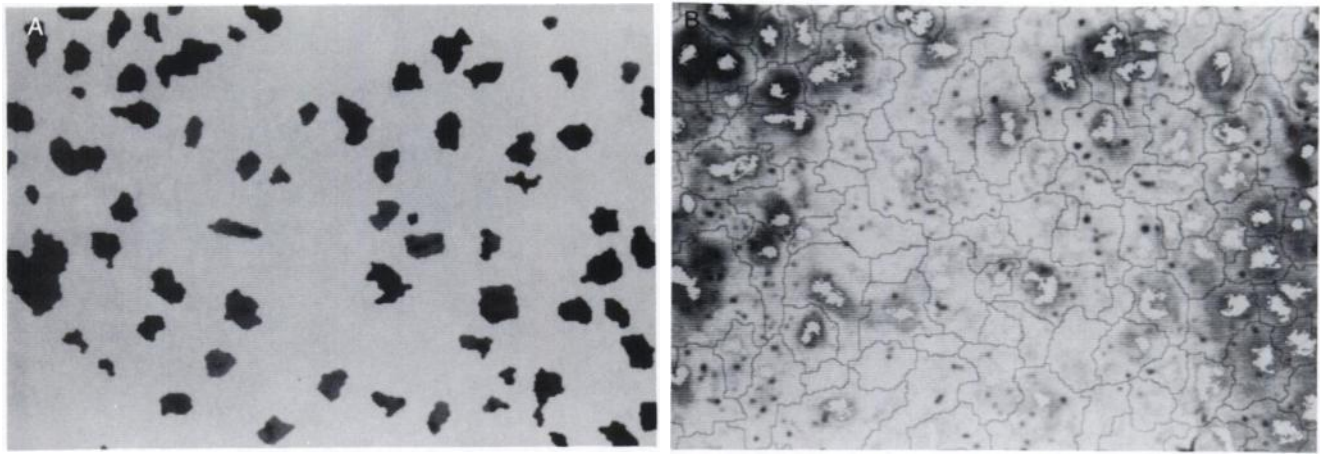


FIGURE 9. (A) The image under the cell nuclei mask only. All pixels not under the mask have been set to a grey level of 255 (white). (B) The image of the background only. All pixels under the mask of the cell nuclei have been set to a grey level of 255 (white).

- From the background image (Fig. 9B), a black top-hat transform is applied. The top-hat transform is a filter which selects only areas from the image of small sharp detail. This transform performs an image opening (erosion followed by dilation of the same magnitude) of the image, and then subtracts the result from the original image. Therefore, if the top-hat kernel is set to two, all features whose centroids are not surrounded by a layer of at least two pixels will be eliminated by the opening operation, and will appear as high contrast features when the opened image is subtracted from the original. This transform is well suited for the extraction of small black objects, such as the silver grains of an autoradiograph. It also results in the detection of single-pixel noise, and fractal detail arising from the nonsmoothed contours of the cell nuclei (Fig. 9A), which were subtracted from the original image in Figure 1A to obtain the background image of Figure 9B.
- A grey level threshold can be set to discriminate all objects extracted by the black top-hat, including noise and fractal detail.
- The application of the minima function on Figure 9B combined with a logic operation between the binary planes containing the grey level threshold data and the image minima, removes fractal artifacts arising from the edges of the cell nuclei.
- Elimination of objects from the detected feature set of size less than 4 pixels removes noise from the image. The remaining features represent the detected extra-nuclear grains.
- From the image of the cell nuclei (Fig. 9A), adjacent pixel smoothing (matrix kernel 2) is used to flatten variations in nuclear stain, without removing the grains.
- Local minima within the cell nuclei are sought to identify potential grains. Minima greater than 4 pixels are counted as grains.
- Overlying the binary planes containing the detected grains from the cell nuclei and the background on the original image gives the resultant image with all detected grains (Fig. 3).

ACKNOWLEDGMENTS

The authors thank Don Lafety from Leica for useful ideas and suggestions regarding the image analysis procedures. This work

was supported by NCI grants R01 CA50886 and R29 CA49017 and by the American Cancer Society grant ACS-PDT-442.

REFERENCES

1. Bernstein ID, Press OW, Eary JF, et al. Treatment of leukemia and lymphoma using antibody labeled with high doses of ^{131}I . *Antib Immunconj Radiopharm* 1991;4:771-776.
2. DeNardo GL, DeNardo SJ, O'Grady LF, Levy NB, Adams GP, Mills SL. Fractionated radioimmunotherapy of B-cell malignancies with ^{131}I Lym-1. *Cancer Res* 1990;50:1014-1016.
3. Sitzmann JV, Order SE, Klein JL, Lechner PK, Fishman EK, Smith GW. Conversion by new treatment modalities of nonresectable hepatocellular cancer. *J Clin Oncol* 1987;5:1566-1573.
4. Stewart JSW, Hird V, Snook D, et al. Intraperitoneal radioimmunotherapy for ovarian cancer: pharmacokinetics, toxicity and efficacy of ^{131}I -labeled monoclonal antibodies. *Int J Radiat Oncol Biol Phys* 1989;16:405-413.
5. Begent R, Ledermann JA, Green AJ, et al. Antibody distribution and dosimetry in patients receiving radiolabelled antibody therapy for colorectal cancer. *Br J Cancer* 1989;60:406-412.
6. Carrasquillo JA, Krohn KA, Beaumier P, et al. Diagnosis of and therapy for solid tumors with radiolabeled antibodies and immune fragments. *Cancer Treat Reports* 1984;68:317-328.
7. Bagshawe KD, Sharma SK, Southall PJ, et al. Selective uptake of toxic nucleoside (^{125}I UdR) by resistant cancer. *Br J Radiol* 1991;64:37-44.
8. Van den Abbeele AD, Baranowska-Kortylewicz J, Adelstein SJ, et al. Diagnostic and therapeutic applications of Auger electron-emitting 5-(^{125}I / ^{125}I)iodo-2'-deoxyuridine in cancer. In: Howell RW, Narra VR, Sastry KSR, Rao DV, eds., *Biophysical aspects of Auger processes*. Woodbury, NY: American Institute of Physics; 1992:372-395.
9. Humm JL, Charlton DE. A new calculational method to assess the therapeutic potential of Auger electron emission. *Int J Radiat Oncol Biol Phys* 1989;17:351-360.
10. Link EM, Carpenter RN. ^{211}At -methylene-blue for targeted radiotherapy of human melanoma xenografts: treatment of micrometastases. *Cancer Res* 1990;50:2963-2967.
11. Link EM, Brown I, Carpenter RN, Mitchell JS. Uptake and therapeutic effectiveness of ^{125}I - and ^{211}At -methylene blue for pigmented melanoma in an animal model system. *Cancer Res* 1989;49:4332-4337.
12. Brown I. Astatine-211: its possible applications on cancer therapy. *Appl Radiat Isot* 1986;37:789-798.
13. McLaughlin WH, Milius RA, Pillai KMR, Edasery JP, Blumenthal RD, Bloomer WD. Cytotoxicity of receptor mediated 16α -(^{125}I)iodo-estradiol in cultured MCF-7 human breast cancer cells. *J Natl Cancer Inst* 1989;81:437-440.
14. Humm JL, Cobb LM. Nonuniformity of tumor dose in radioimmunotherapy. *J Nucl Med* 1990;31:75-83.
15. Humm JL, Chin LM, Cobb LM, Begent R. Microdosimetry in radioimmunotherapy. *Radiat Prot Dosim* 1990;31:433-436.
16. Macklis RM, Lin JY, Beresford B, Atcher RW, Hines JJ, Humm JL.

Cellular kinetics, dosimetry, and radiobiology of α -particle radioimmunotherapy: induction by apoptosis. *Radiat Res* 1992;130:220–226.

17. Griffith MH, Yorke ED, Wessels BW, DeNardo GL, Neacy WP. Direct dose confirmation of quantitative autoradiography with micro-TLD measurements for radioimmunotherapy. *J Nucl Med* 1988;29:1795–1809.
18. Eklund KE, Williams JR. A method for quantitative autoradiography over stained sections of tumors exposed in vivo to radiolabeled antibodies. *Int J Radiat Oncol Biol Phys* 1991;21:1635–1642.
19. Roberson PL, Buchsbaum DJ, Heidorn DB, Ten Haken RK. Three-dimensional tumor dosimetry for radioimmunotherapy using serial autoradiography. *Int J Radiat Oncol Biol Phys* 1992;24:329–334.
20. Rogers AW. *Techniques of autoradiography*, New York: Elsevier Press; 3rd edition. 1979.
21. Serra J. *Image analysis and mathematical morphology*. London: Academic Press Inc.; 1982:415–416.
22. Russ JC. *The image processing handbook*. Boca Raton, FL: CRC Press; 1992:328–330.
23. Giger ML, Doi K, MacMahon H. Image feature analysis and computer-aided diagnosis in digital radiography. 3. Automated detection of nodules in peripheral lung fields. *Med Phys* 1988;15:158–166.
24. Humm JL, Macklis RM, Bump K, Cobb LM, Chin LM. Internal dosimetry using data derived from autoradiography. *J Nucl Med* 1993;34:1811–1817.